

Direct evidence of induced magnetic moment in Se and the role of misplaced Mn in MnBi₂Se₄-based intrinsic magnetic topological insulator heterostructures

R. Fukushima,¹ V. N. Antonov², M. M. Otrokov³, T. T. Sasaki⁴, R. Akiyama,¹ K. Sumida^{5,*}, K. Ishihara,¹ S. Ichinokura¹, K. Tanaka,⁶ Y. Takeda,^{5,†} D. P. Salinas⁷, S. V. Ereemeev⁸, E. V. Chulkov^{9,10,11,12,13}, A. Ernst^{14,‡} and T. Hirahara^{1,‡}

¹*Department of Physics, Tokyo Institute of Technology, Tokyo 152-8551, Japan*

²*Institute for Theoretical Physics, Johannes Kepler University, A-4040 Linz, Austria*

³*Instituto de Nanociencia y Materiales de Aragón (INMA), CSIC-Universidad de Zaragoza, Zaragoza 50009, Spain*

⁴*Research Center for Magnetic and Spintronic Materials, National Institute for Materials Science, Tsukuba 305-0047, Japan*

⁵*Materials Sciences Research Center, Japan Atomic Energy Agency, Sayo, Hyogo 679-5148, Japan*

⁶*UVSOR III Synchrotron, Institute for Molecular Science, Okazaki 444-8585, Japan*

⁷*ALBA Synchrotron Light Source, E-08290 Cerdanyola del Valles, Spain*

⁸*Institute of Strength Physics and Materials Science, Tomsk, 634055, Russia*

⁹*Donostia International Physics Center (DIPC), Paseo de Manuel Lardizabal, 4, 20018 San Sebastián/Donostia, Basque Country, Spain*

¹⁰*Departamento de Física de Materiales, Facultad de Ciencias Químicas, UPV/EHU, Apdo. 1072, 20080 San Sebastián, Basque Country, Spain*

¹¹*Centro de Física de Materiales, CFM-MPC, Centro Mixto CSIC-UPV/EHU, Apdo.1072, 20080 San Sebastián/Donostia, Basque Country, Spain*

¹²*Tomsk State University, Tomsk, 634050, Russia*

¹³*Saint Petersburg State University, Saint Petersburg, 198504, Russia*

¹⁴*Max Planck Institute of Microstructure Physics, D-06120 Halle (Saale), Germany*



(Received 25 April 2024; accepted 24 July 2024; published 15 August 2024)

Intrinsic magnetic topological insulators, in which magnetism and topology are inherently combined, are excellent systems to realize exotic phenomena such as the quantum anomalous Hall effect. However, there are many reports that show that the experimental samples are not so ideal and the effect of the unintentional disorder in these systems needs to be considered carefully. In this study, we investigate the role of misplaced magnetic atoms as well as nonmagnetic elements in the intrinsic magnetic topological insulator heterostructures based on MnBi₂Se₄ and Bi₂Se₃. We find that Mn atoms are not only placed at the central layer of the MnBi₂Se₄ septuple layer (SL) but also intermix with Bi (antisite Mn) as well as reside in the van der Waals (vdW) gap. Through a detailed comparison between the experimental and theoretical x-ray magnetic circular dichroism (XMCD) spectra, we find that the antisite Mn is coupled ferromagnetically, whereas the vdW Mn couple antiferromagnetically to the Mn in the central atomic plane of the SL. Furthermore, we detect a clear XMCD signal in nonmagnetic Se, providing unambiguous evidence of its magnetic interaction with Mn.

DOI: [10.1103/PhysRevMaterials.8.084202](https://doi.org/10.1103/PhysRevMaterials.8.084202)

I. INTRODUCTION

The interplay of magnetism and topological properties [1] leads to exotic quantum phenomena like the quantized anomalous Hall effect (QAHE) [2,3], topological magnetoelectric effect [4], or the half-integer quantum Hall effect [5]. Intrinsic magnetic topological insulators (TIs) such as MnBi₂Te₄ (MBT) are materials that intrinsically possess both magnetic and topologically nontrivial properties. They are experimentally realized both in thin films [6,7] and in the bulk form [8]. Even superlattices composed of magnetic TIs and nonmagnetic TIs have been fabricated [9].

The influence of the native defects, which are misplaced Mn atoms, on the magnetic and electronic structure of the compounds of the MBT family is being actively studied. Both macroscopic [10–12] and local [13] measurements reveal that in MBT and MnSb₂Te₄ the Mn atoms in the central layer of the septuple layer (SL) and those in the Bi/Sb layers couple antiferromagnetically (AFM). According to the recent density functional theory (DFT) calculations [14], this magnetic structure may be responsible for the unexpected reduction of the gap in the surface Dirac cone (DC) of MBT, observed by angle-resolved photoemission spectroscopy (ARPES) [8,15–25]. The gap size fluctuations across the surface have been visualized using scanning tunneling spectroscopy (STS) for the surfaces of the MnBi_{2-x}Sb_xTe₄ bulk single crystals [26] as well as the molecular-beam epitaxy-grown MBT [27,28] and MnSb₂Te₄ [29,30] films. As far as the cousin compound MnBi₂Se₄ (MBS) and heterostructures on its basis are concerned [6,31,32], the coupling of the Mn antisites to the main

*Present address: Research Institute for Synchrotron Radiation Science, Hiroshima University, 2-313 Kagamiyama, Higashi-Hiroshima 739-0046, Japan.

†Deceased.

‡Contact author: hirahara@phys.titech.ac.jp

Mn sites has not been studied yet. Especially, an element-specific as well as a site-specific study that can directly correlate the local magnetic properties of atoms residing at different places of the sample in real space is not thoroughly conducted. Besides, for the intrinsic magnetic TI family, so far there has been no evidence of induced magnetic moments in nonmagnetic elements, although many x-ray magnetic circular dichroism (XMCD) measurements have been performed [8,29,32–37]. This is in contrast to the case of magnetic impurity-doped TIs [38–40].

Therefore, in the present work, we study MBS and characterize the Mn distribution of MBS/Bi₂Se₃ (BS, non-magnetic) and MBS/*n* quintuple layer (QL) BS/MBSBS heterostructures with scanning transmission electron microscopy (STEM) at the atomic scale. Then, this information is correlated with the site-specific magnetic property of the system, focusing on the misplaced Mn and Se atoms obtained with element-specific XMCD measurements. We find that Mn atoms are not only placed at the central layer of the MBS SL, but also intermix with Bi as well as reside in the van der Waals (vdW) gap. By comparing the experimental and theoretical XMCD spectra, it is revealed that the former two couple ferromagnetically (FM) whereas the vdW Mn couple AFM to the Mn in the central atomic plane of the SL. This behavior is different from the case of MBT and is also reproduced by directly calculating the exchange coupling constant. Furthermore, we succeed in detecting a clear XMCD signal in one of the nonmagnetic constituents of the heterostructures — Se, providing unambiguous evidence of its magnetic interaction with Mn.

II. METHODS

The heterostructure samples were prepared by molecular beam epitaxy in ultrahigh vacuum (UHV) chambers equipped with a reflection-high-energy electron diffraction (RHEED) system. First, a clean Si(111)-7 × 7 surface was prepared on an *n*-type substrate by a cycle of resistive heat treatments. The 7 × 7 surface was terminated with Bi, which led to the formation of the Si(111)-√3 × √3 surface. Bi was then deposited on the √3 × √3 surface at ~200 °C in a Se-rich condition. Such a procedure is reported to result in a smooth epitaxial film formation with the stoichiometric ratio of Bi : Se = 2 : 3. The grown Bi₂Se₃ films were annealed at ~250 °C for 5 minutes. The thickness of the Bi₂Se₃ films in this work is ~8 QL. Finally, Mn was deposited on Bi₂Se₃ in a Se-rich condition at ~250 °C. In this process, Mn and Se intercalate into the topmost QL of BS to form the MBSBS heterostructure. The 1 × 1 periodicity with the same lattice constant is maintained during this process for the samples we have fabricated. Then, an additional (*n* + 1) QL of Bi₂Se₃ was deposited on top of the MBSBS, and then Mn and Se were intercalated to form the MBS/*n* QL BS/MBSBS heterostructures [Fig. S1(a)].

For the XMCD and STEM measurements, the fabricated samples were first characterized with ARPES at room temperature. They were then capped with 10 nm of Se before taking them out of the UHV chamber.

For the XMCD measurements, the samples were annealed at ~250 °C to remove the capping layers prior to the measurements. The x-ray absorption spectroscopy (XAS) and XMCD

measurements were performed at BL23SU of SPring-8 [41] and at BL29 BOREAS of ALBA with the total-electron-yield method [42].

Electron transparent specimens for STEM observations were prepared by the standard lift-out technique using an FEI Helios G4-UX dual-beam system. Probe aberration corrected STEM, FEI TitanG2 80–200 microscope, was used. Chemical compositions were measured by energy-dispersive x-ray spectroscopy (EDS). EDS data was obtained for a 2.4 × 7.3 nm² region with a beam size of 100 × 300 pm² that can resolve the layered structure of Mn, Bi, and Te at ~0.2 nm spacing.

Electronic structure calculations were carried out within the DFT, using the projector augmented-wave (PAW) method [43] as implemented in the VASP code [44,45]. The Hamiltonian contained scalar relativistic corrections and the spin-orbit coupling was taken into account by the second variation method [46]. The generalized gradient approximation (GGA-PBE [47]) for the exchange-correlation energy and the DFT-D3 vdW functional with Becke-Johnson damping [48] were applied. The *k*-point mesh of 10 × 10 × 1 was used to sample the slab Brillouin zone. The Mn 3*d*-states were treated, employing the GGA + *U* approach [49] within the Dudarev scheme [50]. The $U_{\text{eff}} = U - J$ value for the Mn 3*d*-states was chosen to be equal to 5.34 eV.

Exchange interactions were studied by applying the magnetic force theorem as it is implemented within the multiple scattering theory [51,52]. For that, the electronic structures of MBT and MBS/BS were calculated using a self-consistent Green's function method within the density functional theory [52,53] within PBESol approximation to the exchange-correlation functional [54]. At that, the Mn 3*d* states were treated employing the GGA + *U* approach [49], the *U* value being equal to 3.5 eV for both MBT and MBSBS. Chemical disorder was modeled by mixing two atomic species on the same atomic site within the coherent potential approximation (CPA) [55,56].

Theoretical XAS and XMCD simulations have been performed using a linear response approach as it is implemented within an LMTO method [57].

To simulate the XAS and XMCD spectra and to calculate the exchange coupling parameters, the position of the Mn atom in the vdW gap has been determined by means of the total-energy calculations done using VASP. We have found that the Mn atom prefers the tetrahedral vdW site [Fig. 1(f)], being located practically within the vdW Se layer of the SL.

III. RESULTS AND DISCUSSIONS

First, we discuss the atomic structure of the samples we have fabricated. Figure 1(a) shows the STEM image of the heterostructure with *n* = 1 and this clearly indicates that the designed structure is formed in this region. However, in Fig. 1(b), which is the STEM image of the *n* = 3 designed sample, one can find structures of *n* = 1, 3, and 4, showing that these samples can be inhomogeneous with regions of different *n* coexisting. Furthermore, areas where the MBS layers are absent as well as regions with three SLs were also observed. A variety of different structures that is observed is shown in Figs. S1(b)–(e) of the Supplemental Material [58]. Thus, our STEM measurements suggest that although the

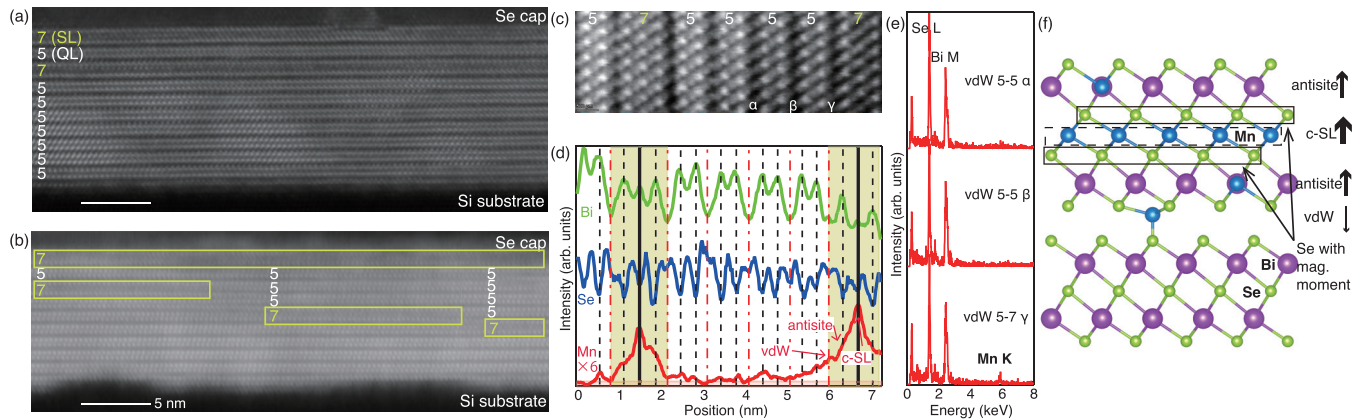


FIG. 1. (a), (b) STEM image of the MBS/ n QL BS/MBSBS sample for $n = 1$ (a) and 3 (b), respectively. (c) Close-up image of the $n = 4$ region seen on the right of panel (b). (d) EDS mapping of (c), showing the chemical composition of the heterostructure. Mn can not only be found in the central layer of the SL (c-SL), but is intermixed with Bi (antisite Mn) as well as reside inside the vdW gap. The Mn spectrum has been enhanced by a factor of six. (e) Energy-dispersive x-ray spectra at the vdW gap of different positions in the sample indicated in (c). Whereas the Mn peak is absent at the vdW gap between 2 QLs, a clear Mn peak can be detected at the SL-QL vdW gap. (f) Schematic drawing of the Mn distribution inside the MBSBS heterostructure. The arrows show the mutual alignments of the local magnetic moments at the three different Mn sites, as deduced from the comparison of measured and calculated XAS and XMCD spectra. The Se layers with finite magnetic moments are also indicated.

heterostructure samples are mostly the same as our original design of Fig. S1(a), other structures can coexist and one needs to take this into account when performing macroscopic measurements. We also found that variation in n was larger for samples designed for larger n . This fact is particularly important to discuss the band structure of these samples as is scrutinized in Figs. S2 and S3.

Next, we concentrate on the actual atomic composition of the heterostructures. Figure 1(c) shows the high-resolution high-angle annular dark field STEM (HAADF-STEM) image taken from the [110] direction of the $n = 4$ region. Figure 1(d) shows the results of EDS measurements. To emphasize the distribution of Mn, the curve for Mn has been multiplied by a factor of six. As anticipated from the original design, Mn mainly lies at the center of the SL (c-SL). The position of Bi and Se seems to be also the same as the designed structure. However, a detailed inspection shows that the width of the Mn peak shown in Fig. 1(d) is broad and not only limited to the center of the SL but extends into the adjacent layers. Particularly, it seems that Mn can intermix in the Bi layers which we will call “antisite Mn.” Furthermore, the Mn signal still seems to be larger than the background intensity even farther away from the center of the SL, extending to the vdW gap between adjacent Se atoms. To verify this characteristic more vividly, Fig. 1(e) shows the EDS spectra at the vdW gap at three different positions of Fig. 1(c). While peaks that correspond to Se L and Bi M transitions can be identified in all the spectra shown, the Mn K peak is only detected at the SL-QL vdW gap. This clearly shows that Mn atoms can reside even in the vdW gap of the heterostructures of MBS and BS. Although magnetic atoms have been known to reside in the vdW gaps for doped samples [62,63], to the best of our knowledge, this is the first experimental observation in the intrinsic magnetic TIs. Figure 1(f) summarizes the present findings. Ideally, Mn should only reside at the center of the MBS SL, but experimentally it can intermix with Bi as well as reside in the vdW gap.

As discussed above, it is known that the misplaced Mn atoms alter the magnetic property of the intrinsic magnetic TI. Therefore, to clarify the magnetic interaction between the different Mn sites, we performed XMCD measurements. Figure 2(a) shows the XAS spectra taken at 6 K with a magnetic field of 5 T applied perpendicular to the sample at the Mn L edge for the MBS/7 QL BS/MBSBS sample. μ_+ and μ_- correspond to the spectrum obtained with left- and right-handed circularly polarized photons, respectively. The corresponding XMCD spectrum is also shown and a clear signal is detected both at the L_3 and L_2 edges. The XMCD intensity has been deduced by normalizing $\mu_+ - \mu_-$ with the magnitude of the peak intensity at the L_3 edge [the difference of the values of the averaged XAS spectrum at 635 eV (background), and at 640 eV (peak position)].

We now compare the averaged XAS and XMCD data with theory to verify the magnetism of Mn at different sites. As shown in Fig. S4, the shape of the XMCD spectra did not change significantly for different heterostructure samples as well as for different measurement conditions. This is probably because the spot size in the XMCD measurements is $\sim 200 \mu\text{m}$ and regions with different n coexist in all the samples as well as the fact that the concentration of the misplaced Mn is nearly the same since the same sample fabrication procedure is employed. Thus, we performed the calculation of the XAS and XMCD spectra for a single septuple layer MBS and compared to the experimental data. Figures 2(b)–2(d) show the XAS and XMCD spectra for the Mn in the central atomic plane of the SL (b), at the Bi site (c), and in the vdW gap (d), respectively. The Mn valence in these sites is +2, +2, and +3, respectively. For the antisite Mn and Mn at the vdW gap, the Mn portion was set at 10%. It can be easily noticed that the experimental data in Fig. 2(a) cannot be reproduced by considering c-SL Mn alone [Fig. 2(b)] and one needs to consider Mn at different sites. To be more specific, the former can only show a single peak for the L_2 edge, whereas in the experiment there are clearly two peaks. Quantitatively, we

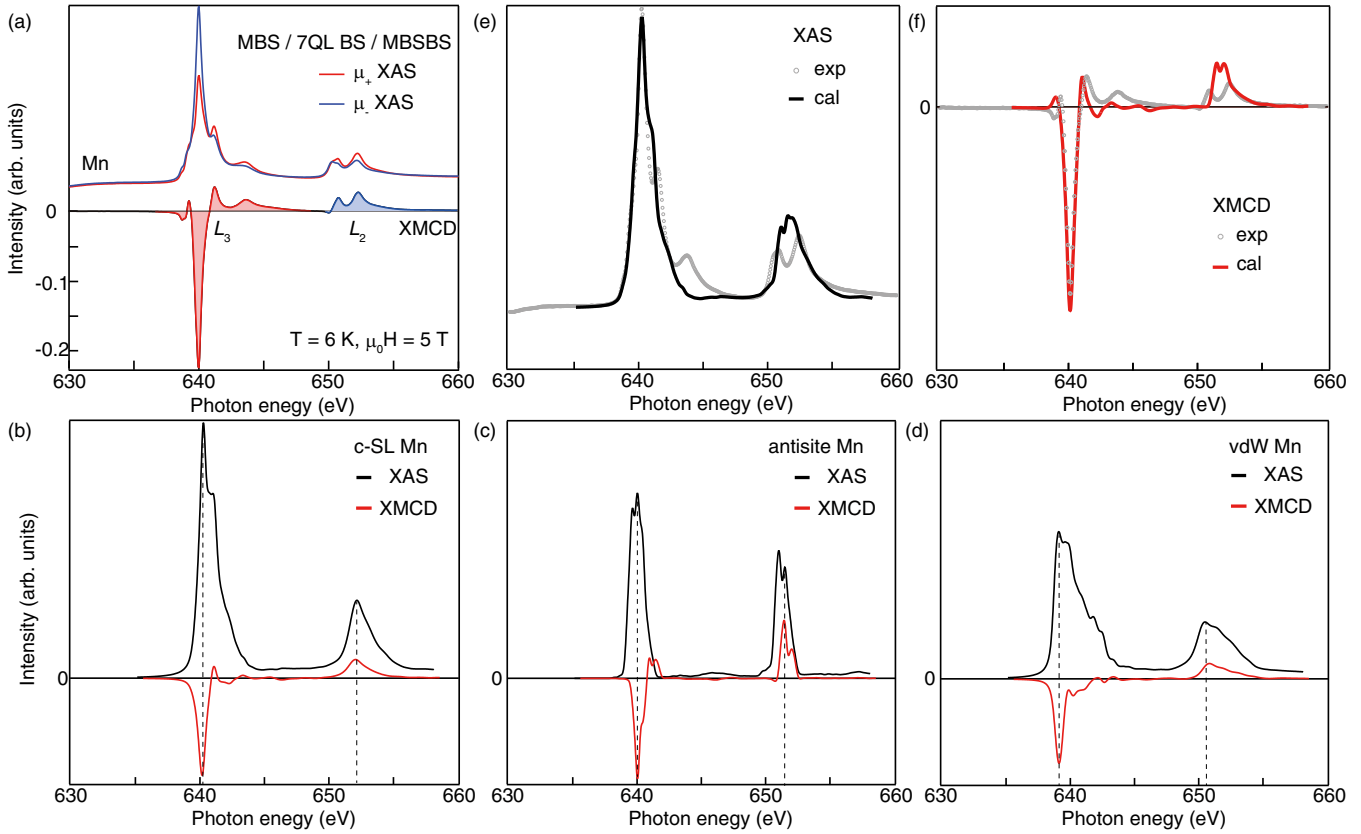


FIG. 2. (a) X-ray absorption spectra (XAS) measured at 6 K for a circularly polarized incident light when a magnetic field of 5 T was applied along the sample surface-normal direction for the MBS/7 QL BS/MBSBS heterostructure at the Mn L edge. μ_+ and μ_- correspond to the spectrum obtained with left and right-handed circularly polarized photons, respectively. The corresponding XMCD spectrum is also shown. (b)–(d) Calculated XAS and XMCD spectra for the Mn at the central layer in the SL (b), the Mn intermixed with Bi (antisite Mn) (c), and the Mn in the vdW gap (d), respectively. (e) Comparison of the experimental and calculated XAS spectra. The calculated spectrum is the convolution of the spectra shown in (b)–(d) with a ratio of 7 : 2 : 1. (f) Comparison of the experimental and calculated XMCD spectra. The calculated spectrum is the convolution of the spectra shown in (b)–(d) with a ratio of 7 : 2 : -1.

notice that the energy position of the largest XMCD signal is not the same for different Mn sites, as indicated by the dotted lines in Figs. 2(b)–2(d).

We have tried to convolute the calculated spectra of the three different Mn sites and reproduce the experimental XAS and XMCD curves, as shown in Figs. 2(e) and 2(f). We could not obtain a perfect match, but the overall consistency was good when the ratio between the three Mn components of Figs. 2(b)–2(d) was 6-7 : 3-2 : 1 for the XAS spectra (Fig. S5) [64]. The spectrum shown in Fig. 2(e) is the case for a ratio of 7 : 2 : 1, whereas it is 7 : 2 : -1 in the XMCD spectrum in Fig. 2(f). The meaning of the plus (minus) sign is that the magnetic coupling is FM (AFM). Comparison of the experimental and convoluted theoretical XMCD spectra for various magnetic coupling scenarios is shown in Fig. S5. The important conclusion from this analysis is that the antisite Mn is coupled FM to the c-SL Mn whereas the vdW Mn is AFM coupled to the former two [Fig. 1(f)]. This is contrary to the case of MBT, where the c-SL Mn and antisite Mn were shown to couple AFM and can diminish the DC gap in the band dispersion [14].

To verify if this conclusion can be reproduced by a different approach, we have calculated the Heisenberg exchange

coupling constants directly using the magnetic force theorem for MBT and MBS/BS, as shown in Fig. 3. The exchange interactions of the c-SL Mn with antisite Mn atoms in MBT and MBSBS, as well as with the vdW Mn atoms in MBSBS, are shown. Note that the patterns of the $J_{0j}(r_{0j})$ dependence for the two systems are different because there are no Mn atoms in the vdW gap in the MBT case. It can be seen from the figure that in both systems the J_{01} parameters are positive, indicating FM coupling between the nearest neighbors inside the c-SL Mn layers. However, for the interactions between the c-SL and antisite Mn atoms the opposite signs of J_{0j} are revealed. While in MBT these parameters are negative (J_{02} and J_{03}), indicating the AFM coupling in agreement with experiment [11,13], in MBSBS they are positive (J_{02} and J_{04}), meaning the FM coupling. Moreover, for MBSBS, the AFM coupling between the c-SL Mn and that in the vdW gap is revealed, as both J_{03} and J_{05} are negative. Thus, the results of the magnetic force theorem calculations for the c-SL Mn coupling to the antisite and vdW Mn are in agreement with the conclusions drawn from the fitting of the experimental XMCD curves by the calculated ones.

To elucidate why the signs of the exchange integrals for the couplings with antisites in MBSBS are opposite to those

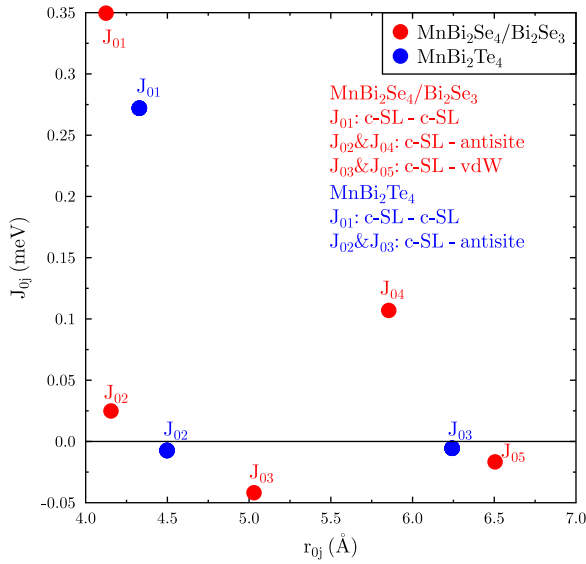


FIG. 3. Calculated Heisenberg exchange coupling constants J_{0j} for the Mn-Mn pair interactions as a function of the distance $r_{\text{Mn}(c\text{-SL})\text{-Mn}(j)}$ for MBT (blue circles) and MBSBS (red circles). The interactions with the atoms from the neighboring SL blocks are not shown. As indicated in the legend, the c-SL-antisite interactions are described by J_{02} and J_{03} in MBT, while in MBSBS they correspond to J_{02} and J_{04} . This is because in MBSBS there are Mn atoms in the vdW gap, their couplings to c-SL Mn being described by J_{03} and J_{05} .

of MBT, we have further analyzed the electronic densities of states. As can be seen in Fig. 4, the hybridization of the antisite Mn $3d$ states with the Bi and Se states in MB-SBS is stronger than that with Bi and Te states in MBT. The stronger hybridization can be explained by shorter interatomic distances in MBSBS that, as a result, enhances indirect

double-exchange interaction between the local magnetic moments.

Now we will try to unveil the role of the nonmagnetic elements in these systems. Since measuring small XMCD signals for nonmagnetic elements is known to be extremely difficult [37,65,66], we have performed careful XAS/XMCD measurements at 6 K with a magnetic field of 10 T applied perpendicular to the sample at the Se L edge for the MBS/7 QL BS/MBSBS sample, as shown in Fig. 5(a). The XMCD intensity has been deduced by normalizing $\mu_+ - \mu_-$ with the magnitude of the peak intensity at the L_3 edge [the difference of the value of the averaged XAS spectrum at 1431 eV (background) and 1447 eV (peak)]. One can notice that finite XMCD signals arise at the L_3 and L_2 absorption edges. It seems that the peak structure is complex and the signal for both edges contains a pair of positive and negative peaks. To show that this signal is not an artifact, we show the Se XMCD spectra for different samples as well as the spectrum measured at different conditions in a separate facility in Fig. 5(b). Qualitatively, we can say that the prominent pair peak structure for different samples is the same and we are sure that this signal is a real signal of Se magnetization. Compared to the results of similar measurements performed at the same beamline in SPring-8 (Ref. [65]) or ALBA (Ref. [66]) that report the absence of XMCD signals at the Se L edge, we are sure that the signals observed are finite and not an artifact. We emphasize that this kind of XMCD signal in nonmagnetic elements has been reported for Heusler alloys [67] or magnetic impurity-doped TIs [38–40]. However, this is the first example of a clear detection of the magnetic moment of a nonmagnetic element in intrinsic magnetic TIs, directly showing the magnetic interaction with the Mn layer. We also note that a very unclear XMCD signal was detected at the Bi N edge ($4d \rightarrow 6p$) as shown in Fig. S6 and the reason for this may be that the peak signal of the XAS spectra itself is quite weak in Bi.

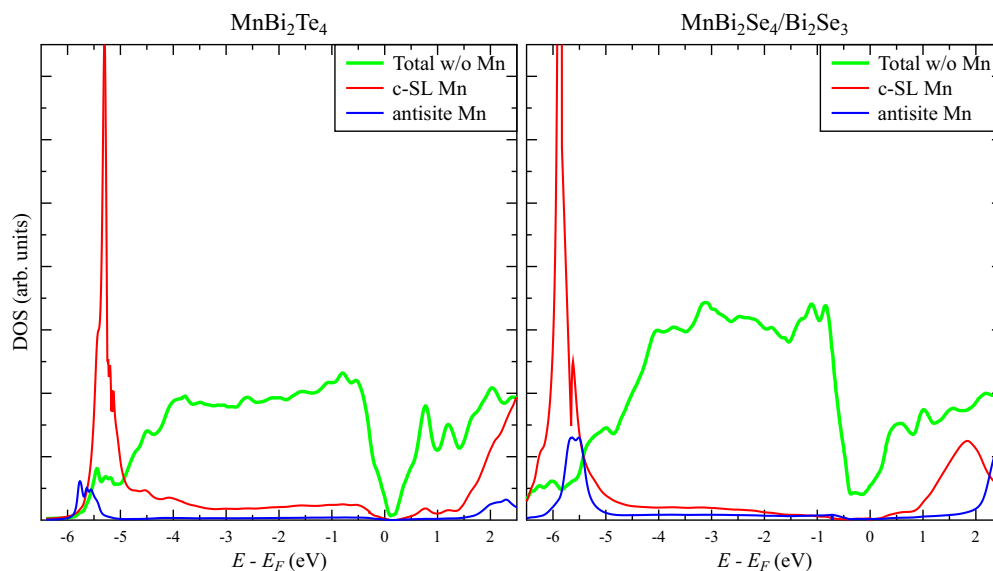


FIG. 4. Calculated density of states (DOS) of MBT (left) and MBSBS (right). The green curves show the sums of the projected DOSs of all Bi and Se atoms, while the red and blue ones show the projected DOSs of c-SL Mn and antisite Mn, respectively. The calculations are made taking spin-orbit coupling into account.

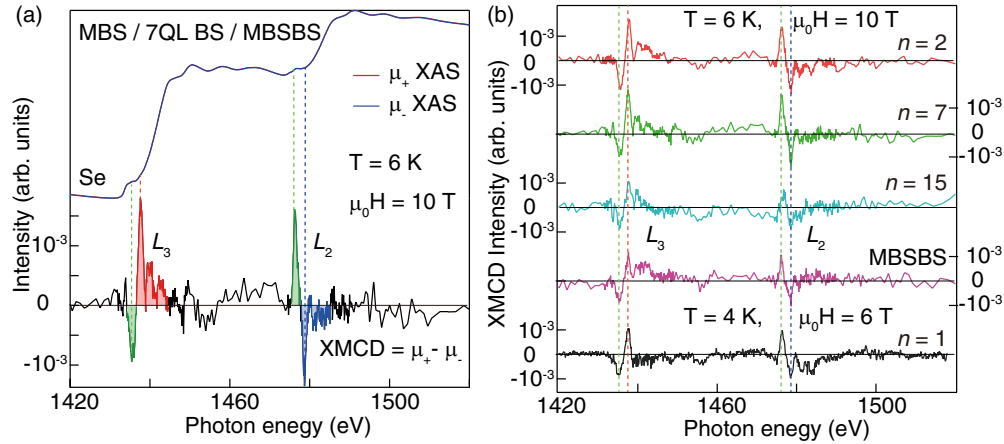


FIG. 5. (a) X-ray absorption spectra (XAS) measured at 6 K for a circularly polarized incident light when a magnetic field of 10 T was applied along the sample surface-normal direction for the MBS/7 QL BS/MBSBS heterostructure at the Se L edge. The corresponding XMCD spectrum is also shown, indicating the clear detection of the Se magnetization. The red and blue main peaks likely correspond to the $2p \rightarrow 4d$ transition and the green pre-edge peaks correspond to the $2p \rightarrow 4s$ transition. (b) Comparison of the XMCD spectra between the MBS/ n QL BS/MBSBS heterostructures for $n = 1, 2, 7, 15$ and that of MBSBS.

By carefully comparing the XAS and XMCD spectra, one notices that the peak at lower photon energy in the XMCD spectrum appears prior to the main absorption for both the L_3 and L_2 edges, as colored in green. These pre-edge peaks are opposite in sign with the main peaks colored in red and blue and moreover, their intensity is nearly the same order of magnitude as the main peaks. In addition, the sign of the XMCD signal is the opposite between the Mn and Se for the main peaks, thus suggesting that the Mn and Se are AFM coupled, consistent with what has been theoretically predicted in Ref. [6].

Figure 6(a) compares the experimental XAS data subtracted by the background with the calculation for the Se L edge [67]. The Se in this case corresponds to the atoms in the layer adjacent to the central plane of the SL (i.e., Mn) and not those composing the vdW gap, as shown in Fig. 1(f). Although the calculation shows fine features not observed in the experiment, we can say that the two are consistent concerning the largest peaks. Figure 6(b) shows the comparison between the experimental and calculated XMCD signals. Again, the consistency between the two is good, further reinforcing the fact that the experimentally observed signal at the Se L edge is not an artifact. However, the pre-edge signal is somewhat weaker for the calculated spectrum.

Since the main peak of the L edge should correspond to the $2p \rightarrow 4d$ transition, it is possible that the pre-edge peak which is at ~ 2 eV smaller photon energy with opposite sign, includes the contribution from the $2p \rightarrow 4s$ transition, since the change of the angular momentum in the transition is the opposite between $2p \rightarrow 4d$ (+1) and $2p \rightarrow 4s$ (-1). To test the above hypothesis, we first compare the calculated XAS spectrum with the calculated spin-integrated unoccupied partial density of state (PDOS) of the Se orbitals in the single MBS SL. Figure 6(c) shows the comparison between the XAS spectrum and the PDOS of Se $4s$ and $4d$ for the L_3 edge. The energy position has been shifted so that the spectral features of the $4d$ DOS and XAS will coincide with each other. One can notice that the DOS of the s orbitals is much smaller than the d orbitals, and furthermore, the peak position of the s orbital is

at a smaller energy than the peaks for the d orbital. Figure 6(d) compares the calculated XMCD spectrum with the DOS difference between the majority and minority spin for the s and d orbitals. The DOS difference, which corresponds to the spin polarization of Se, is very small for both the s and d orbitals but finite values can be found at energies that are close to the peak positions in the XMCD spectrum. We can definitely say that the main peak originates from the spin polarization of the $4d$ states. For the pre-edge peak, although it is difficult to say that the spin-polarization of the s orbitals is giving the main

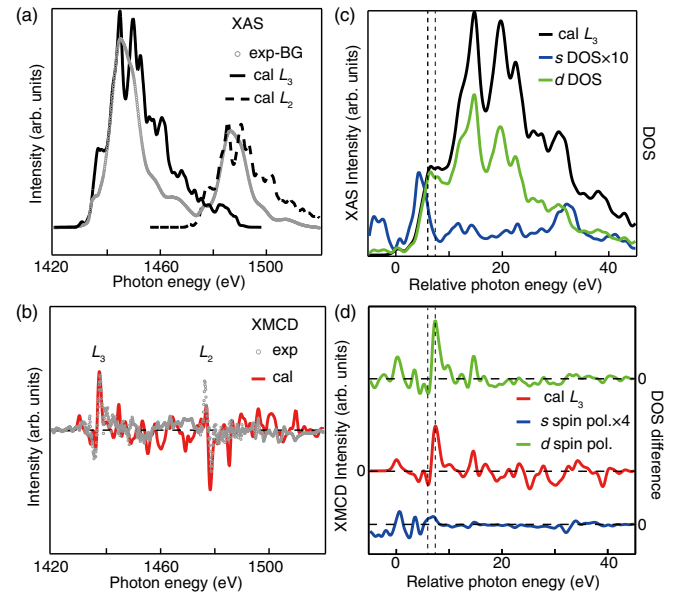


FIG. 6. (a), (b) Comparison of the experimental XAS (a) and XMCD (b) spectra with the calculation at the Se L edge. (c) Comparison of the calculated XAS spectrum of the Se L_3 edge with the partial DOS of Se $4s$ and $4d$ orbitals. (d) Comparison of the calculated XMCD spectrum of the Se L_3 edge with the spin polarization (difference of the partial DOS of the majority and minority state) of Se $4s$ and $4d$ orbitals.

contribution, its contribution should be larger than the main peak, considering the larger DOS shown in Fig. 6(c). Thus, we conclude that the main feature of the XMCD spectra of Se can be basically understood by the PDOS of the Se orbitals, and the slight discrepancy between the experimental and theoretical XMCD spectra should originate from the difference in the actual contribution of the *s* orbitals.

IV. CONCLUSION

In summary, we performed STEM and XMCD measurements on MBS/*n* QL BS/MBSBS heterostructures and found that the Mn atoms are not placed only in the central SL of MBS, but intermix with Bi as well as reside in the vdW gap. By comparing the experimentally measured XMCD spectra with theory, we find that the *c*-SL Mn and the antisite Mn are coupled ferromagnetically, whereas the vdW Mn is most likely coupled antiferromagnetically with the former two, which is different from the case of MBT. We also found clear evidence of the magnetic interaction of the Mn and Se from the detection of the XMCD signal at the Se *L* edge. These results suggest the importance of identifying the magnetism of each element in different environments in the intrinsic magnetic TIs.

ACKNOWLEDGMENTS

We thank P. Gargiani and M. Valvidares for their assistance with the XMCD experiments. T.H. acknowledges the

support by Grants-In-Aid from Japan Society for the Promotion of Science (Grants No. 18H03877 and No. 22H00293), the Murata Science Foundation (Grant No. H30-084), the Asahi Glass Foundation, the Iketani Science and Technology Foundation (Grant No. 0321083-A), and Support for Tokyo Tech Advanced Researchers. M.M.O. acknowledges the support by MCIN/AEI/10.13039/501100011033/ (Grant No. PID2022-138210NB-I00) and “ERDF A way of making Europe,” by Ayuda CEX2023-001286-S financiada por MICIU/AEI/10.13039/501100011033, as well as MCIN with funding from European Union NextGenerationEU (PRTR-C17.I1) promoted by the Government of Aragon. S.V.E. acknowledges support from the Government research assignment for ISPMS SB RAS, project FWRW-2022-0001. E.V.C. acknowledges Saint-Petersburg State University for research Project 95442847. The ARPES measurements were performed under the UVSOR Proposals No. 21-681, No. 21-867, No. 22IMS6661, and No. 22IMS6856. The XMCD measurements were performed at JAEA beamline BL-23SU in SPring-8 (Proposals No. 2020A3843, No. 2021A3843, and No. 2021B3843) and BL-29 BOREAS in ALBA (Proposal No. 2023027296). The work at SPring-8 was performed under the Shared Use Program of JAEA Facilities (Proposals No. 2020A-E16, No. 2021A-E19, and No. 2021B-E16) with the approval of Nanotechnology Platform project supported by the Ministry of Education, Culture, Sports, Science and Technology (Proposals No. JPMXP09A20AE0016, No. JPMXP09A21AE0017, and No. JPMXP09A21AE0036).

-
- [1] Y. Tokura, K. Yasuda, and A. Tsukazaki, *Nat. Rev. Phys.* **1**, 126 (2019).
- [2] F. D. M. Haldane, *Phys. Rev. Lett.* **61**, 2015 (1988).
- [3] C. Z. Chang, J. Zhang, X. Feng, J. Shen, Z. Zhang, M. Guo, K. Li, Y. Ou, P. Wei, L. L. Wang, Z. Q. Ji, Y. Feng, S. Ji, X. Chen, J. Jia, X. Dai, Z. Fang, S. C. Zhang, K. He, Y. Wang, L. Lu, X. C. Ma, and Q. K. Xue, *Science* **340**, 167 (2013).
- [4] X.-L. Qi, T. L. Hughes, and S.-C. Zhang, *Phys. Rev. B* **78**, 195424 (2008).
- [5] M. Mogi, Y. Okamura, M. Kawamura, R. Yoshimi, K. Yasuda, A. Tsukazaki, K. S. Takahashi, T. Morimoto, N. Nagaosa, M. Kawasaki, Y. Takahashi, and Y. Tokura, *Nat. Phys.* **18**, 390 (2022).
- [6] T. Hirahara, S. V. Ereemeev, T. Shirasawa, Y. Okuyama, T. Kubo, R. Nakanishi, R. Akiyama, A. Takayama, T. Hajiri, S. Ideta, M. Matsunami, K. Sumida, K. Miyamoto, Y. Takagi, K. Tanaka, T. Okuda, T. Yokoyama, S. Kimura, S. Hasegawa, and E. V. Chulkov, *Nano Lett.* **17**, 3493 (2017).
- [7] T. Hirahara, M. M. Otrokov, T. T. Sasaki, K. Sumida, Y. Tomohiro, S. Kusaka, Y. Okuyama, S. Ichinokura, M. Kobayashi, Y. Takeda, K. Amemiya, T. Shirasawa, S. Ideta, K. Miyamoto, K. Tanaka, S. Kuroda, T. Okuda, K. Hono, S. V. Ereemeev, and E. V. Chulkov, *Nat. Commun.* **11**, 4821 (2020).
- [8] M. M. Otrokov, I. I. Klimovskikh, H. Bentmann, D. Estyunin, A. Zeugner, Z. S. Aliev, S. Gaß, A. U. B. Wolter, A. V. Koroleva, A. M. Shikin, M. Blanco-Rey, M. Hoffmann, I. P. Rusinov, A. Yu. Vyazovskaya, S. V. Ereemeev, Y. M. Koroteev, V. M. Kuznetsov, F. Freyse, J. Sánchez-Barriga, I. R. Amiraslanov, M. B. Babanly, N. T. Mamedov, N. A. Abdullayev, V. N. Zverev, A. Alfonsov, V. Kataev, B. Büchner, E. F. Schwier, S. Kumar, A. Kimura, L. Petaccia, G. D. Santo, R. C. Vidal, S. Schatz, K. Kißner, M. Inzelmann, C. H. Min, S. Moser, T. R. F. Peixoto, F. Reinert, A. Ernst, P. M. Echenique, A. Isaeva, and E. V. Chulkov, *Nature (London)* **576**, 416 (2019).
- [9] I. I. Klimovskikh, M. M. Otrokov, D. Estyunin, S. V. Ereemeev, S. O. Filnov, A. Koroleva, E. Shevchenko, V. Voroshnin, A. G. Rybkin, I. P. Rusinov, M. Blanco-Rey, M. Hoffmann, Z. S. Aliev, M. B. Babanly, I. R. Amiraslanov, N. A. Abdullayev, V. N. Zverev, A. Kimura, O. E. Tereshchenko, K. A. Kokh, L. Petaccia, G. D. Santo, A. Ernst, P. M. Echenique, N. T. Mamedov, A. M. Shikin, and E. V. Chulkov, *npj Quantum Mater.* **5**, 54 (2020).
- [10] Y. Liu, L.-L. Wang, Q. Zheng, Z. Huang, X. Wang, M. Chi, Y. Wu, B. C. Chakoumakos, M. A. McGuire, B. C. Sales, W. Wu, and J. Yan, *Phys. Rev. X* **11**, 021033 (2021).
- [11] Y. Lai, L. Ke, J. Yan, R. D. McDonald, and R. J. McQueeney, *Phys. Rev. B* **103**, 184429 (2021).
- [12] S. X. M. Riberolles, Q. Zhang, Elijah Gordon, N. P. Butch, Liqin Ke, J.-Q. Yan, and R. J. McQueeney, *Phys. Rev. B* **104**, 064401 (2021).
- [13] M. Sahoo, I. Onuorah, L. Folkers, E. Chulkov, M. Otrokov, Z. Aliev, I. Amiraslanov, B. Büchner, L. Corredor, C. Wang, Z. Salman, A. Isaeva, R. De Renzi, and G. Allodi, *Adv. Sci.* **e2402753** (2024).

- [14] M. Garnica, M. M. Otrokov, P. C. Aguilar, I. I. Klimovskikh, D. Estyunin, Z. S. Aliev, I. R. Amiraslanov, N. A. Abdullayev, V. N. Zverev, M. B. Babanly, N. T. Mamedov, A. M. Shikin, A. Arnau, A. L. V. de Parga, E. V. Chulkov, and R. Miranda, *npj Quantum Mater.* **7**, 7 (2022).
- [15] E. D. L. Rienks, S. Wimmer, J. Sánchez-Barriga, O. Caha, P. S. Mandal, J. Růžička, A. Ney, H. Steiner, V. V. Volobuev, H. Groiss, M. Albu, G. Kothleitner, J. Michalička, S. A. Khan, J. Minár, H. Ebert, G. Bauer, F. Freyse, A. Varykhalov, O. Rader, and G. Springholz, *Nature (London)* **576**, 423 (2019).
- [16] Y. Gong, J. Guo, J. Li, K. Zhu, M. Liao, X. Liu, Q. Zhang, L. Gu, L. Tang, X. Feng, D. Zhang, W. Li, C. Song, L. Wang, P. Yu, X. Chen, Y. Wang, H. Yao, W. Duan, Y. Xu, S.-C. Zhang, X. Ma, Q.-K. Xue, and K. He, *Chin. Phys. Lett.* **36**, 076801 (2019).
- [17] J. Wu, F. Liu, M. Sasase, K. Ienaga, Y. Obata, R. Yukawa, K. Horiba, H. Kumigashira, S. Okuma, T. Inoshita, and H. Hosono, *Sci. Adv.* **5**, eaax9989 (2019).
- [18] Y.-J. Hao, P. Liu, Y. Feng, X.-M. Ma, E. F. Schwier, M. Arita, S. Kumar, C. Hu, R. Lu, M. Zeng, Y. Wang, Z. Hao, H.-Y. Sun, K. Zhang, J. Mei, N. Ni, L. Wu, K. Shimada, C. Chen, Q. Liu, and C. Liu, *Phys. Rev. X* **9**, 041038 (2019).
- [19] H. Li, S.-Y. Gao, S.-F. Duan, Y.-F. Xu, K.-J. Zhu, S.-J. Tian, J.-C. Gao, W.-H. Fan, Z.-C. Rao, J.-R. Huang, J.-J. Li, D.-Y. Yan, Z.-T. Liu, W.-L. Liu, Y.-B. Huang, Y.-L. Li, Y. Liu, G.-B. Zhang, P. Zhang, T. Kondo, S. Shin, H.-C. Lei, Y.-G. Shi, W.-T. Zhang, H.-M. Weng, T. Qian, and H. Ding, *Phys. Rev. X* **9**, 041039 (2019).
- [20] Y. J. Chen, L. X. Xu, J. H. Li, Y. W. Li, H. Y. Wang, C. F. Zhang, H. Li, Y. Wu, A. J. Liang, C. Chen, S. W. Jung, C. Cacho, Y. H. Mao, S. Liu, M. X. Wang, Y. F. Guo, Y. Xu, Z. K. Liu, L. X. Yang, and Y. L. Chen, *Phys. Rev. X* **9**, 041040 (2019).
- [21] B. Chen, F. Fei, D. Zhang, B. Zhang, W. Liu, S. Zhang, P. Wang, B. Wei, Y. Zhang, Z. Zuo, J. Guo, Q. Liu, Z. Wang, X. Wu, J. Zong, X. Xie, W. Chen, Z. Sun, S. Wang, Y. Zhang, M. Zhang, X. Wang, F. Song, H. Zhang, D. Shen, and B. Wang, *Nat. Commun.* **10**, 4469 (2019).
- [22] P. Swatek, Y. Wu, L.-L. Wang, K. Lee, B. Schrunk, J. Yan, and A. Kaminski, *Phys. Rev. B* **101**, 161109(R) (2020).
- [23] S. H. Lee, Y. Zhu, Y. Wang, L. Miao, T. Pillsbury, H. Yi, S. Kempinger, J. Hu, C. A. Heikes, P. Quarterman, W. Ratcliff, J. A. Borchers, H. Zhang, X. Ke, D. Graf, N. Alem, C.-Z. Chang, N. Samarth, and Z. Mao, *Phys. Rev. Res.* **1**, 012011(R) (2019).
- [24] A. M. Shikin, T. P. Makarova, A. V. Eryzhenkov, D. Y. Usachov, D. A. Estyunin, D. A. Glazkova, I. I. Klimovskikh, A. G. Rybkin, and A. V. Tarasov, *Physica B: Condens. Matter* **649**, 414443 (2023).
- [25] A. M. Shikin, D. A. Estyunin, N. L. Zaitsev, D. Glazkova, I. I. Klimovskikh, S. O. Filnov, A. G. Rybkin, E. F. Schwier, S. Kumar, A. Kimura, N. Mamedov, Z. Aliev, M. B. Babanly, K. Kokh, O. E. Tereshchenko, M. M. Otrokov, E. V. Chulkov, K. A. Zvezdin, and A. K. Zvezdin, *Phys. Rev. B* **104**, 115168 (2021).
- [26] F. Lüpke, M. Kolmer, J. Yan, H. Chang, P. Vilmercati, H. H. Weitering, W. Ko, and A.-P. Li, *Commun. Mater.* **4**, 82 (2023).
- [27] M. Liu, C. Lei, H. Kim, Y. Li, L. Frammolino, J. Yan, A. H. Macdonald, and C. K. Shih, *Proc. Natl. Acad. Sci. USA* **119**, e2207681119 (2022).
- [28] Q. Li, I. D. Bernardo, J. Maniatis, D. McEwen, A. Dominguez-Celorio, M. T. H. Bhuiyan, M. Zhao, A. Tadich, L. Watson, B. Lowe, T.-H.-Y. Vu, C. X. Trang, J. Hwang, S.-K. Mo, M. S. Fuhrer, and M. T. Edmonds, *Adv. Mater.* **36**, 2312004 (2024).
- [29] S. Wimmer, J. Sanchez-Barriga, P. Kuppers, A. Ney, E. Schierle, F. Freyse, O. Caha, J. Michalicka, M. Liebmann, D. Primetzhofer, M. Hoffmann, A. Ernst, M. M. Otrokov, G. Bihlmayer, E. Weschke, B. Lake, E. V. Chulkov, M. Morgenstern, G. Bauer, G. Springholz, and O. Rader, *Adv. Mater.* **33**, 2102935 (2021).
- [30] P. Kuppers, J. Zenner, S. Wimmer, G. Springholz, O. Rader, M. Liebmann, and M. Morgenstern, *arXiv:2202.11540*.
- [31] R. C. Walko, T. Zhu, A. J. Bishop, R. K. Kawakami, and J. A. Gupta, *Physica E* **143**, 115391 (2022).
- [32] T. Zhu, A. J. Bishop, T. Zhou, M. Zhu, D. J. O'Hara, A. A. Baker, S. Cheng, R. C. Walko, J. J. Repicky, T. Liu, J. A. Gupta, C. M. Jozwiak, E. Rotenberg, J. Hwang, I. Zutic, and R. K. Kawakami, *Nano Lett.* **21**, 5083 (2021).
- [33] A. M. Shikin, D. A. Estyunin, I. I. Klimovskikh, S. O. Filnov, E. F. Schwier, S. Kumar, K. Miyamoto, T. Okuda, A. Kimura, K. Kuroda, K. Yaji, S. Shin, Y. Takeda, Y. Saitoh, Z. S. Aliev, N. T. Mamedov, I. R. Amiraslanov, M. B. Babanly, M. M. Otrokov, S. V. Eremeev, and E. V. Chulkov, *Sci. Rep.* **10**, 13226 (2020).
- [34] P. Kagerer, C. I. Fornari, S. Buchberger, T. Tschirner, L. Veyrat, M. Kamp, A. V. Tcakaev, V. Zabolotnyy, S. L. Morelhão, B. Geldiyev, S. Müller, A. Fedorov, E. Rienks, P. Gargiani, M. Valvidares, L. C. Folkers, A. Isaeva, B. Büchner, V. Hinkov, R. Claessen, H. Bentmann, and F. Reinert, *Phys. Rev. Res.* **5**, L022019 (2023).
- [35] P. Kagerer, C. I. Fornari, S. Buchberger, S. L. Morelhão, R. C. Vidal, A. Tcakaev, V. Zabolotnyy, E. Weschke, V. Hinkov, M. Kamp, B. Büchner, A. Isaeva, H. Bentmann, and F. Reinert, *J. Appl. Phys.* **128**, 135303 (2020).
- [36] R. C. Vidal, A. Zeugner, J. I. Facio, R. Ray, M. H. Haghghi, A. U. B. Wolter, L. T. C. Bohorquez, F. Caglieris, S. Moser, T. Figgemeier, T. R. F. Peixoto, H. B. Vasili, M. Valvidares, S. Jung, C. Cacho, A. Alfonsov, K. Mehlawat, V. Kataev, C. Hess, M. Richter, B. Büchner, J. van den Brink, M. Ruck, F. Reinert, H. Bentmann, and A. Isaeva, *Phys. Rev. X* **9**, 041065 (2019).
- [37] A. Tcakaev, B. Rubrecht, J. I. Facio, V. B. Zabolotnyy, L. T. Corredor, L. C. Folkers, E. Kochetkova, T. R. F. Peixoto, P. Kagerer, S. Heinze, H. Bentmann, R. J. Green, P. Gargiani, M. Valvidares, E. Weschke, M. W. Haverkort, F. Reinert, J. van den Brink, B. Büchner, A. U. B. Wolter, A. Isaeva, and V. Hinkov, *Adv. Sci.* **10**, 2203239 (2023).
- [38] M. Ye, T. Xu, G. Li, S. Qiao, Y. Takeda, Y. Saitoh, S.-Y. Zhu, M. Nurmamat, K. Sumida, Y. Ishida, S. Shin, and A. Kimura, *Phys. Rev. B* **99**, 144413 (2019).
- [39] M. Ye, W. Li, S. Zhu, Y. Takeda, Y. Saitoh, J. Wang, H. Pan, M. Nurmamat, K. Sumida, F. Ji, Z. Liu, H. Yang, Z. Liu, D. Shen, A. Kimura, S. Qiao, and X. Xie, *Nat. Commun.* **6**, 8913 (2015).
- [40] M. F. Islam, C. M. Canali, A. Pertsova, A. Balatsky, S. K. Mahatha, C. Carbone, A. Barla, K. A. Kokh, O. E. Tereshchenko, E. Jiménez, N. B. Brookes, P. Gargiani, M. Valvidares, S. Schatz, T. R. F. Peixoto, H. Bentmann, F. Reinert, J. Jung, T. Bathon, K. Fauth, M. Bode, and P. Sessi, *Phys. Rev. B* **97**, 155429 (2018).

- [41] Y. Saitoh, Y. Fukuda, Y. Takeda, H. Yamagami, S. Takahashi, Y. Asano, T. Hara, K. Shirasawa, M. Takeuchi, T. Tanaka, and H. Kitamura, *J. Synchrotron Radiat.* **19**, 388 (2012).
- [42] A. Barla, J. Nicolás, D. Cocco, S. M. Valvidares, J. Herrero-Martín, P. Gargiani, J. Moldes, C. Ruget, E. Pellegrin, and S. Ferrer, *J. Synchrotron Radiat.* **23**, 1507 (2016).
- [43] P. E. Blöchl, *Phys. Rev. B* **50**, 17953 (1994).
- [44] G. Kresse and J. Furthmüller, *Phys. Rev. B* **54**, 11169 (1996).
- [45] G. Kresse and D. J. Joubert, *Phys. Rev. B* **59**, 1758 (1999).
- [46] D. D. Koelling and B. N. Harmon, *J. Phys. C* **10**, 3107 (1977).
- [47] J. P. Perdew, K. Burke, and M. Ernzerhof, *Phys. Rev. Lett.* **77**, 3865 (1996).
- [48] S. Grimme, S. Ehrlich, and L. Goerigk, *J. Comput. Chem.* **32**, 1456 (2011).
- [49] V. I. Anisimov, J. Zaanen, and O. K. Andersen, *Phys. Rev. B* **44**, 943 (1991).
- [50] S. L. Dudarev, G. A. Botton, S. Y. Savrasov, C. J. Humphreys, and A. P. Sutton, *Phys. Rev. B* **57**, 1505 (1998).
- [51] A. I. Liechtenstein, M. I. Katsnelson, V. P. Antropov, and V. A. Gubanov, *J. Magn. Magn. Mater.* **67**, 65 (1987).
- [52] M. Hoffmann, A. Ernst, W. Hergert, V. N. Antonov, W. A. Adeagbo, R. M. Geilhufe, and H. B. Hamed, *Physica Status Solidi (b)* **257**, 1900671 (2020).
- [53] M. Geilhufe, S. Achilles, M. A. Köbis, M. Arnold, I. Mertig, W. Hergert, and A. Ernst, *J. Phys.: Condens. Matter* **27**, 435202 (2015).
- [54] J. P. Perdew, A. Ruzsinszky, G. I. Csonka, O. A. Vydrov, G. E. Scuseria, L. A. Constantin, X. Zhou, and K. Burke, *Phys. Rev. Lett.* **100**, 136406 (2008).
- [55] P. Soven, *Phys. Rev.* **156**, 809 (1967).
- [56] B. L. Gyorffy, *Phys. Rev. B* **5**, 2382 (1972).
- [57] V. N. Antonov, B. N. Harmon, and A. N. Yaresko, *Electronic Structure and Magneto-Optical Properties of Solids* (Springer, Dordrecht, 2004).
- [58] See Supplemental Material at <http://link.aps.org/supplemental/10.1103/PhysRevMaterials.8.084202> for details of the sample atomic structure, the band dispersion measured by ARPES in comparison to DFT calculations, and the details of the XMCD analysis concerning the Mn *L* edge, and the XAS and XMCD spectra for Bi. It also contains Refs. [59–61].
- [59] S. Kimura, T. Ito, M. Sakai, E. Nakamura, N. Kondo, T. Horigome, K. Hayashi, M. Hosaka, M. Katoh, T. Goto, T. Ejima, and K. Soda, *Rev. Sci. Instrum.* **81**, 053104 (2010).
- [60] Y. Sakamoto, T. Hirahara, H. Miyazaki, S. Kimura, and S. I. Hasegawa, *Phys. Rev. B* **81**, 165432 (2010).
- [61] Y. Zhang, K. He, C.-Z. Chang, C.-L. Song, L.-L. Wang, X. Chen, J.-F. Jia, Z. Fang, X. Dai, W.-Y. Shan, S.-Q. Shen, Q. Niu, X.-L. Qi, S.-C. Zhang, X.-C. Ma, and Q.-K. Xue, *Nat. Phys.* **6**, 584 (2010).
- [62] M. M. Yee, Z.-H. Zhu, A. Soumyanarayanan, Y. He, C.-L. Song, E. Pomjakushina, Z. Salman, A. Kanigel, K. Segawa, Y. Ando, and J. E. Hoffman, *Phys. Rev. B* **91**, 161306(R) (2015).
- [63] J. Růžička, O. Caha, V. Holý, H. Steiner, V. Volobuev, A. Ney, G. Bauer, T. Duchoň, K. Veltruská, I. Khalakhan, V. Matolín, E. F. Schwier, H. Iwasawa, K. Shimada, and G. Springholz, *New J. Phys.* **17**, 013028 (2015).
- [64] The reason for the absence of a perfect match may be that the XMCD calculations have been done in a single-particle picture while in reality, there should be many-body effects as well as clustering of the Mn atoms in the experiment. Furthermore, theory assumes broadening of the peak structure with finite lifetime, and this is not easy to predict perfectly. This is particularly significant at ~ 644 eV in Fig. 2(e); whereas only a shoulder structure is seen for the calculation, it shows up as a clear peak in the experimental XAS data. Even when a more sophisticated calculation method is employed for a pure system, the theoretical and experimental XMCD spectra cannot be perfectly matched, eg. *Phys. Rev. Lett.* **132**, 176701 (2024).
- [65] K. Sumida, Y. Takeda, S. Kusaka, K. Kobayashi, and T. Hirahara, *Phys. Rev. Mater.* **6**, 014006 (2022).
- [66] A. I. Figueroa, F. Bonell, M. G. Cuxart, M. Valvidares, P. Gargiani, G. van der Laan, A. Mugarza, and S. O. Valenzuela, *Phys. Rev. Lett.* **125**, 226801 (2020).
- [67] T. Yoshikawa, V. N. Antonov, T. Kono, M. Kakoki, K. Sumida, K. Miyamoto, Y. Takeda, Y. Saitoh, K. Goto, Y. Sakuraba, K. Hono, A. Ernst, and A. Kimura, *Phys. Rev. B* **102**, 064428 (2020).